Dear Author:

Please find attached the final pdf file of your contribution, which can be viewed using the Acrobat Reader, version 3.0 or higher. We would kindly like to draw your attention to the fact that copyright law is also valid for electronic products. This means especially that:

- You may not alter the pdf file, as changes to the published contribution are prohibited by copyright law.

- You may print the file and distribute it amongst your colleagues in the scientific community for scientific and/or personal use.

- You may make your article published by Springer-Verlag available on your personal home page provided the source of the published article is cited and Springer-Verlag is mentioned as copyright holder. You are requested to create a link to the published article in Springer's internet service. The link must be accompanied by the following text: The original publication is available at http://link.springer.de or at http://link.springer-ny.com . Please use the appropriate URL and/or DOI for the article. Articles disseminated via SpringerLink are indexed, abstracted and referenced by many abstracting and information services, bibliographic networks, subscription agencies, library networks and consortia.

- Without having asked Springer-Verlag for a separate permission your institute/your company is not allowed to place this file on its homepage.

- Please address any queries to the production editor of the journal in question, giving your name, the journal title, volume and first page number.

Yours sincerely,

Springer-Verlag

REPORT

E. Isoun · C. Fletcher · N. Frazer · J. Gradie

Multi-spectral mapping of reef bathymetry and coral cover; Kailua Bay, Hawaii

Abstract We used high-resolution, airborne, digital, multi-spectral imagery to map bathymetry and the percent of living coral in the nearshore marine environment of Kailua Bay, Oahu, Hawai'i. Three spectral bands, with centers at 488, 551, and 577 nm (each with a full-width half maximum of 10 nm), were selected for good water transmission and good coral/sand/algae discrimination. However, the third band (577 nm) was not used in the depth and bottom-type solutions. The spatial resolution of 1 m per pixel was selected to balance resolution with the size of the total data set. A radiative transfer model accounting for the optical effects of the atmosphere, ocean surface, water, and reflection off the ocean bottom substrates was applied to the multi-spectral images, normalizing multiple images to one another for a mosaic that spans the bay. Atmospheric parameters in the radiative transfer model were estimated from published values measured for similar environments. Water-attenuation coefficients for the model were determined from the observed spectral data values over the sand bottom type in the bay. Relative depth and bottom-type coefficients were derived by a method most simply described as the "differencing" of two spectral bands. Accuracy exceeding 85% in predicted depth was achieved to a depth of 25 m. Depth prediction errors were assessed with comparison to hydrographic survey data. Classification of bottom-type coefficients into seven "percent living coral" categories results in 77% overall accuracy tested by diver-obtained line-intercept transect data (ground truth). Bottom-type coefficients derived by the model were corrected for atmospheric and ocean conditions on the date of collection, so spatial changes in bathymetry and "percent living coral" through time can be analyzed and related to environmental factors. The radiative transfer model and the "differencing" method used to solve for depth and "percent living coral" can be applied to any airborne, passive remote sensing digital data with appropriate spectral bands.

Keywords Multi-spectral · Modeling · Bathymetry · Reef · Pacific · Nearshore · Mapping · Hawaii

E. Isoun · C. Fletcher (✉) · N. Frazer
Department of Geology and Geophysics,
School of Ocean and Earth Science and Technology,
University of Hawaii, 1680 East-West Road,
P.O. Box 721, Honolulu, Hawai'i 96822, USA
E-mail: fletcher@soest.hawaii.edu
Tel.: +1-808-9562582
Fax: +1-808-9565512

J. Gradie
STI Services, Inc., 733 Bishop St., Suite 3100,
Honolulu, HI 96813, USA

Introduction

Reef-dominated coasts present unique considerations for mapping with remote sensing data. Ocean water is generally clear, but clarity is dependent on local and seasonal weather conditions. Clear water means sunlight is minimally attenuated and there is reflectance off the ocean floor at depths up to approximately 25 m. Airborne multi-spectral sensors can be flown when weather conditions are good and during hours of maximum sunlight transmittance into the ocean. Low contrast in bottom features occurs in the complex microhabitats that characterize coral–algal reef tracts. With the ability to select narrow electromagnetic wavelength bands for measurement in multi-spectral remote sensing, the potential to discriminate among low-contrast reef features is increased. Spectral discrimination is increased (compared to satellite multi-spectral data) not only by the higher resolution of airborne data, but also by the reduced amount of atmosphere between the sensor and the ocean. The versatility in selecting wavelengths to be measured, flexibility with time of data collection, and good signal-to-noise ratio of multi-spectral sensors make them cost-effective (Green et al. 1996) and optimal for mapping shallow, carbonate, marine environments. The purpose of this research is to estimate the predictive

capability of multi-spectral data. Mapped depth predictions are error-assessed with hydrographic survey data over a section of the multi-spectral mosaic. Line-intercept transect ground truth data are used to determine the accuracy of percent living coral (PLC) predictions.

Passive remote sensing

Passive remote sensors measure reflected sunlight in a given width of the electromagnetic spectrum. Sunlight energy measured over shallow water has been transmitted down through the atmosphere, ocean surface, and water column and reflected off the ocean floor back up through the ocean and through some of the atmosphere. To obtain information about depth and bottom type, radiative transfer equations have been written to include all these interactions (Lyzenga 1978; Paredes and Spero 1983; Philpot 1989). Those parameters that have the greatest effect on the sunlight measured at the sensor have been identified (Gordon and Brown 1974; Gordon 1989; Gregg and Carder 1990; Kirk 1991), although the unknowns must be measured in situ, or approximated from published measurements (Elterman 1968; Maracci 1985) and calculations (Gordon and Brown 1973; Gordon and McCluney 1975; Lyzenga 1977).

The remote sensing reflectance model of Lee et al. (1994) predicts depth using bottom reflectance measured in vivo and measured and calculated values for ocean parameters. In this paper we will estimate depth without the aid of bottom-reflectance measurements. Without correcting the multi-spectral data for depth, confusion over bottom type occurs (Mumby et al. 1998; Holden and LeDrew 1999). For example, at a given wavelength pixels over a highly reflective sandy bottom in deep water may have the same value as pixels over a darker bottom in shallow water.

In this paper, a single scattering radiative transfer model (no downward reflection at the air–water interface) (Philpot 1989) is used to normalize the multi-spectral images by correcting for the effects of the atmosphere and changing solar altitude. Depth and bottom type are predicted by a subtractive method in two bands. Water-attenuation coefficients are determined from normalized multi-spectral pixel values for sand where depth is known. Atmospheric parameters are estimated from the literature and our data set.

Study site

Kailua Bay is a carbonate reef-dominated embayment located on southeast Oahu, Hawai'i (Fig. 1). Two large categories of benthic substrate are found in Kailua Bay: (1) areas of carbonate sand and fossil reef hardgrounds, and (2) reef habitats of coral and algae species. The sand and fossil reef areas show up as light-colored, highly reflective areas in the multi-spectral image mosaic
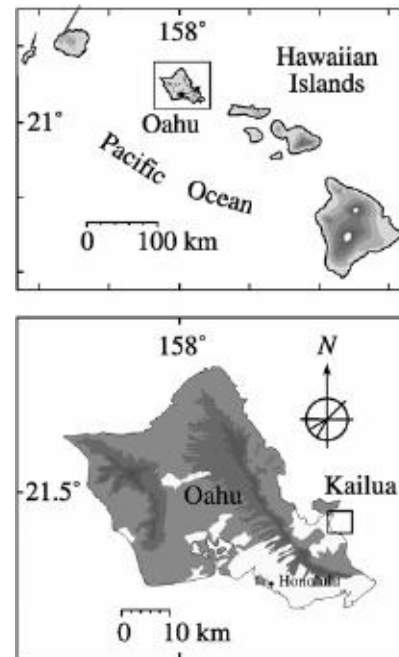

Fig. 1 Location map of Kailua Bay, Oahu, Hawaii

(Fig. 2) and the coral and algae communities are found in the dark-colored, low-reflectance areas of the mosaic.

At the center of the Bay is a sand-floored channel formed from the meandering course of a submerged paleostream. This sand channel cuts across the reef connecting seaward and nearshore sand fields. There are steep bathymetric slopes along the sand channel and reef front. Coral and algae grow on spur-and-groove surface morphology south of the sand channel, and on paleo-shorelines and karst caves and caverns north of the channel (Harney et al. 2000). In other areas north of the channel, there is less submarine topography, and corals and algae grow on plains. Sand fields are scattered throughout the bay.

Dominant winds in Kailua Bay are northeasterly to easterly trades and prevail at speeds averaging 15 knots 70–80% of the year. Winds are reduced for weeks at a time in the wake of southerly low-pressure cells. Winter storms in the North Pacific produce long period swell (up to 2 m) in the bay.

Materials and methods

Data collection

On 10 January 1998, the multi-spectral images for this study were collected from a low-flying (1,400-m high) aircraft. Winds were light, there had been no rain for several days, and there was minimal ocean swell. The data were collected between 9:30 and 10:30 a.m. when sun zenith angles were less than 40°. Water visibility was good, with divers able to see 20–30 m horizontally. With minimal surface and water column perturbation, the ocean bottom was visible to a depth of 30 m from a small boat.

The multi-spectral images were acquired over flight lines running a northwest to southeast transect to optimize coverage of the

Fig. 2 One-meter resolution, multi-spectral image mosaic. *Light-colored* (highly reflective) areas are sand and fossil reef. *Dark features* (composed of various reflectance signals) are areas where habitats of coral and algae occur. A sand-filled, submerged paleostream channel cuts across the center of the reef. Spur-and-groove reef morphology, sand fields, and submerged paleokarst features show up clearly in the multi-spectral mosaic. *Blue color* on land is the extent of the multi-spectral image mosaic. The aerial photograph shows up beneath the multi-spectral mosaic (where houses are a *brown* shade)
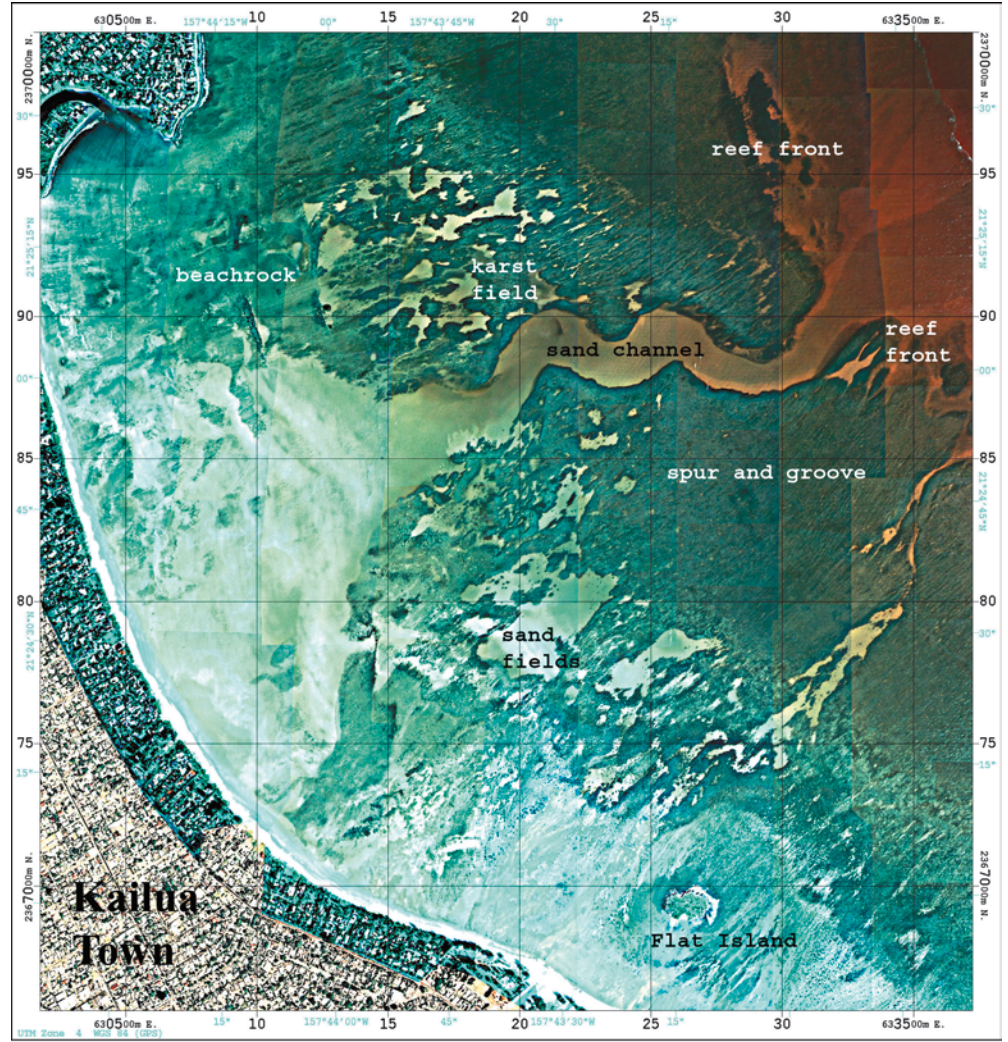
Bay. A 60% overlap in the images was maintained along the flight lines and 20% between parallel scenes. The Application Specific Multi-Spectral Camera System (STI, Inc.) used in this study has 8-bit precision for radiance measurements. Each image, at 1-m resolution, is 578×740 pixels.

Spectral filters used in this study were centered at 488, 551, and 577 nm, each with a full-width half-maximum of 10 nm. Hochberg and Atkinson (2000) recommended these wavelengths as optimal for discrimination of coral reef bottom types. By analyzing spectral field radiometer measurements of coral and algae species and sand in Hawaii, Hochberg and Atkinson identified significant spectral peaks and determined wavelengths that best separate these bottom types. Well-defined peaks due to bottom features were observed by calculating the fourth derivative of high-resolution field radiometer measured spectra. Multivariate techniques of stepwise selection of wavelengths and discriminant function analysis (DFA) were used to determine which wavelength bands best separate coral, algae, and sand.

Data processing

Multi-spectral image georeferencing, modeling, classification, and processing were performed using PCI Geomatics remote sensing and GIS software packages. A multi-spectral map was generated by georegistering and mosaicking each multi-spectral image to an orthorectified coastal aerial photograph with a scale of 1:5,000.

Ground control points collected along the Kailua Bay coastline were used to orthorectify the aerial photograph with an RMS error of 0.5 m (Coyne et al. 1999).

Depth and bottom type by band difference

From the simple equation for the wavelength- (i) dependent radiance measured at the multi-spectral detector, $L_d(i)$

$$L_d(i) = L_b(i) \exp^{-g(i)z} + L_w(i) \tag{1}$$

a derivative band (X) for a given wavelength is defined as

$$X_i \equiv \ln(L_d - L_w) = \ln L_b - gz \tag{2}$$

where L_w is the radiance of the ocean, L_b is the radiance of the ocean bottom, g is a product of the water-attenuation coefficient (κ) and a geometric factor (D) for sunlight ($D = \left(\frac{1}{\cos\theta_{sun}} + \frac{1}{\cos\theta_{cam}}\right)$), and z is depth. We elaborate on Eq. (1) in the Appendices. The equations to solve for depth and bottom type described in the following paragraphs are new ideas proposed and tested in this study.

Solving for bottom type

Recalling Eq. (2), we see that there is one data point (X_i) and two unknowns, $\ln L_b(i)$ and z; therefore the inverse problem is not well

posed. The approach used in this study is, instead of trying to find $\ln L_b(i)$ at each pixel, to solve for the differences in $\ln L_b$ between bands (i,j). Then

$$X_i = \ln L_b(i) - g(i)z$$

$$X_j = \ln L_b(j) - g(j)z$$

and $g(j)X_i - g(i)X_j = g(j) \ln L_b(i) - g(i) \ln L_b(j)$ is a "depth-independent parameter," i.e., a parameter that depends only on bottom type. With three bands, there are three depth-independent bottom parameters (Y) possible in the form

$$Y_{ij} = g(i)X_j - g(j)X_i. \tag{3}$$

Where it is the case that the bottom radiance is the same in two bands (or that the difference is negligible), a scaled version of the depth-independent parameter, Y_{ij}, is the radiance, $\ln L_b$, for a given bottom type. In this case,

$$X_i = \ln L_b - g(i)z$$

$$X_j = \ln L_b - g(j)z.$$

So

$$\ln L_b = \frac{Y_{ij}}{g_i - g_j} = \frac{g_i X_j - g_j X_i}{g_i - g_2}. \tag{4}$$

Solving for depth

For each two-band combination, we estimate depth by a similar approach. In this case

$$X_j - X_i = -g(j)z + g(i)z = (g(i) - g(j))z,$$

and

$$z_{ij} = \frac{X_j - X_i}{g_i - g_j}. \tag{5}$$

The bottom radiance, $\ln L_b$, for the bands used in this study is not independent of band; however, we find that the mean of the depth estimates (z_{ij}) is appropriately bottom independent and that the depth-independent bottom parameter (Y_{ij}) correlates well with bathymetry from a hydrographic survey.

The approach we use assumes that water quality is homogeneous throughout the study area, i.e., that water-attenuation

coefficients κ do not vary in space. This assumption is a simplified way of addressing the depth and bottom-type solution problem. The appropriateness of this assumption is addressed in the "Results" section of this paper.

Applying the model

Wavelength-dependent parameters are estimated from the literature or from multi-spectral data statistics (Table 1). The total optical extinction coefficient for the atmosphere from the ocean surface to space $(\tau_{0-\infty} = \tau'_A + \tau'_R + \tau'_{Oz})$ is 0.529 km^{-1} for the 488-nm band, 0.379 km^{-1} for the 551-nm band, and 0.351 km^{-1} for the 577-nm band. For the atmosphere between the ocean surface and the height of the airplane, the sum of optical extinction coefficients $(\tau_{0-h} = \tau_A + \tau_R + \tau_{Oz})$ is 0.136 km^{-1} for the 488-nm band, 0.125 km^{-1} for the 551-nm band, and 0.116 km^{-1} for the 577-nm band (Elterman 1968). The downwelling irradiance, F_0, is approximately 2 W m^{-2} nm^{-1} for all wavelengths measured (Gregg and Carder 1990). Haze radiance, H, is the value of the offset of the histogram over the multi-spectral mosaic after the bands have been divided by the downwelling irradiance $E_d(0^+)$ and the atmospheric transmittance to the camera A_{T_c} (Eq. A5). H values range from 24–34 W m^{-2} nm^{-1} sr^{-1} for multi-spectral bands 488, 551, and 577 nm.

Water-attenuation coefficients κ are determined from pixel values over sand where depth is known. We use the linear equation that describes the relationship among the product of measured depth z and the distribution function D, and a derivative band X_i (Eq. 2) (Fig. 3). The slope of the linear equation is the water-attenuation coefficient $\kappa(i)$. The intercept is the bottom reflectance, $\ln L_b(i)$, for sand at the given wavelength i. Calculated in this way, water-attenuation coefficients range from 0.05–0.07 m^{-1} for 488–577 nm. These values agree with water-attenuation coefficients calculated from irradiance measurements in the ocean near Tahiti of 0.05–0.08 m^{-1} for Landsat-TM-1 at 450–520 nm (Maritorena 1996). The ocean radiance, L_w, is taken from the L_d (Eq. A5) of pixels over infinitely deep water, where there is no reflectance from the ocean floor (Philpot 1989). L_w is 5, 3, and 5 W m^{-2} nm^{-1} sr^{-1} for bands 488 nm, 551 nm, and 577 nm, respectively.

Incident sun angles are calculated from the Astronomical Almanac for 1998. Other non-wavelength-dependent or sun-angle-dependent parameters calculated or estimated are shown in Table 2. The fraction of downwelling irradiance due to the direct

Table 1 Estimated values for the unknown, wavelength-dependent or non-sun-angle-dependent parameters used in this study

Variable	Symbol	Wavelength (nm)			Units and comments	Reference
		488	551	577		
Optical extinction coefficients	τ'_A	0.264	0.250	0.237	km^{-1} for distance from ocean surface to space	Elterman (1968)
	τ'_R	0.145	0.098	0.069		
	τ'_{Oz}	0.012	0.031	0.045		
	τ_A	0.120	0.114	0.108	km^{-1} for distance from ocean surface to height of airplane (0 to $-h_c$)	
	τ_R	0.016	0.011	0.008		
	τ_{Oz}	0	0	0		
Extraterrestrial irradiance	F_0	1.9371	1.9371	1.9195	W m^{-2} nm^{-1}	Gregg and Carder (1990)
Haze	H	24	34	28	W m^{-2} nm^{-1} sr^{-1} Histogram offset after multi-spectral images corrected for $E_d(0^+)$ and A_{T_c} (Eq. A5)	
Water-attenuation coefficient	κ	0.05	0.07	0.07	m^{-1} Slope of linear regression of corrected pixels over sand to depth (X_i, Eq. 2)	
Deep-water radiance	R_∞	5	3	5	W m^{-2} nm^{-1} sr^{-1} L_d for pixels over deep water (Eq. A5)	Philpot (1989)

component of light f is estimated at 0.66, for >30 km atmospheric visibility (Gregg and Carder 1990). The distribution function for the underwater light field, D, is the sum of the downwelling distribution, D_d, and upwelling distribution, D_u, functions. The diffuse downwelling distribution, D_{d_sky}, is approximately 1.2 (Gordon 1989) and the direct downwelling distribution, D_{d_sun}, is $\frac{1}{\cos\theta_{sw}}$. The total downwelling distribution function, D_d, is the sum of the fractions of the diffuse D_{d_sky} and direct D_{d_sun} components, i.e., $D_d = fD_{d\_sun} + (1-f)D_{d\_sky}$. The upwelling distribution function D_u is composed of the direct component of light only and is given by $\frac{1}{\cos\theta_{cw}}$.

$T(a \rightarrow w)$, the transmission coefficient for downwelling irradiance across the air–water interface, is composed of two distributions, a direct distribution, T_{sun}, and a diffuse distribution, T_{sky}. For direct rays and incident angles $<40°$, the transmission coefficient is well approximated by one minus the Fresnel reflectance $r(\theta_{sa} \rightarrow \theta_{sw})$ (Gregg and Carder 1990). T_{sky}, the transmission coefficient for diffuse irradiance, is approximated by a constant, 0.934, for low wind speeds (Burt 1954). The total downwelling transmission across the air–water interface is given by $T(a \rightarrow w) = fT_{sun} + (1-f)T_{sky}$. The upwelling transmission coefficient at the air–water interface is composed of the direct component alone, so $t(\theta_{cw} \rightarrow \theta_{ca}) = 1 - r(\theta_{cw} \rightarrow \theta_{ca})$. The conversion factor for irradiance to radiance, Q, is equal to π, assuming that the ocean floor is a diffuse reflector. The refractive index of ocean water n_w is 1.335 (Mobley 1994).

Error assessment for predicted depth

Fifteen-meter spatial resolution hydrographic depth data (USGS) were used to assess the error of the depth predictions. Percent error in predicted depth is determined as follows:

$$\text{Percent error} = \left(\frac{\text{``multi} - \text{spectral predicted depth''} - \text{``hydrographic survey depth''}}{\text{``hydrographic survey depth''}} \right) \times 100$$

As the multi-spectral data are at a greater resolution than the hydrographic survey depth data, the mean and median of percent error, reported in the "Results" section of this paper, are determined from multi-spectral predicted depth values only where there are measured hydrographic survey points.

However, for the qualitative, visual comparison of mapped depth shown in the "Results" section, a 15×15-m median filter was applied to the multi-spectral depth prediction map instead of re-sampling the image map to 15-m resolution. Resampling the multi-spectral predicted-depth map results in a blocky data field. Using a median filter preserves the spatial detail of bottom geometry. The hydrographic survey map is made by plotting measured depths onto a grid. The points on the 1-m grid without data are assigned values by interpolation. The grid is converted to image data.

Accuracy assessment for percent living coral

Fourty four "percent living coral" (PLC) population measurements (Harney 2000) were used as ground reference data for bottom-type predictions. These PLC measurements were made using a 30-m line-intercept transect method. In this method, every change in the composition of the ocean bottom is recorded along the transect line. A given PLC category is determined as the fraction of living coral analyzed at this interval compared to all other bottom types observed along the transect. Harney measured living coral to the species level in her study. With this detailed species data, we can discuss coral ecology along with the analysis of our multi-spectral results.

Accuracy in predicted PLC to line-intercept transect data was determined quantitatively using matrix analysis (Table 1). Three accuracies will be reported in the results section of this paper:

(1) the overall accuracy, and the accuracy of individual PLC categories, (2) the producers' accuracy, and (3) the users' accuracy (Congalton and Green 1999).

1. Overall accuracy is calculated as the sum of correctly classified sample units (sum of major diagonal elements) divided by the total number of sample units in the error matrix.
2. Producers' accuracy determines how well a category can be distinguished. It is calculated as the number of correctly clustered pixels (diagonal totals) divided by the total number of reference points in that category (column totals).
3. Users' accuracy shows the percent area of a given class that is actually in that class on the ground. The users' accuracy is computed by dividing the total number of correct pixels in a category (diagonal totals) by the number of pixels classified into that category class (row totals).

The multi-spectral PLC map is filtered with a 29×29-m median filter for the same reason described in the "Error assessment for predicted depth" section of this paper.

### Justification for resolution of ground-truth data

The minimum discernable unit (MDU) (Bainbridge and Reichelt 1988) determines the radiometric precision in predicted depth and PLC. Although the spatial resolution of multi-spectral images in this study is 1 m, spectral mixing from neighboring pixels, and during translation of pixels in georectification of images, means that the ability to make discrete units from the data is lower than the resolution of the data. For the 1-m multi-spectral data used in this study, the MDU $Size_{MDU} = Pixel\ size(1 + 2 \times Error\ Location)$ is 2–7 m. The size of ground reference data should not be smaller than the MDU of the remotely sensed data being tested. The 15-m resolution hydrographic survey data used to assess the error in predicted depth is twice the upper MDU, and the 30-m line-intercept transect data used to assess the PLC maps are four times the upper MDU for the multi-spectral data we collected. This means that it is appropriate to use these reference data to assess the error of depth and PLC predictions in this study.

Results

High-resolution bathymetry and PLC maps were generated for Kailua Bay, Oahu, from a mosaic of multi-spectral images, using radiative transfer methods described in this paper. Contrast-stretched, multi-spectral image maps provided a qualitative method to distinguish highly reflective sand and fossil reef from less reflective living coral and coralline algae habitats, and to outline large submarine geologic features and textures. These maps, in a geographic information system (GIS) format, can be used for fieldwork, as base maps for other scientific studies (e.g., Harney et al. 2000), and for management of reefs (e.g., Maragos and Grober-Dunsmore 1998).

Where images overlap, the measured radiance is not the same due to variations in solar path-length, intensity, and atmospheric conditions. Estimated parameters are fine-tuned using the relative difference in overlapping
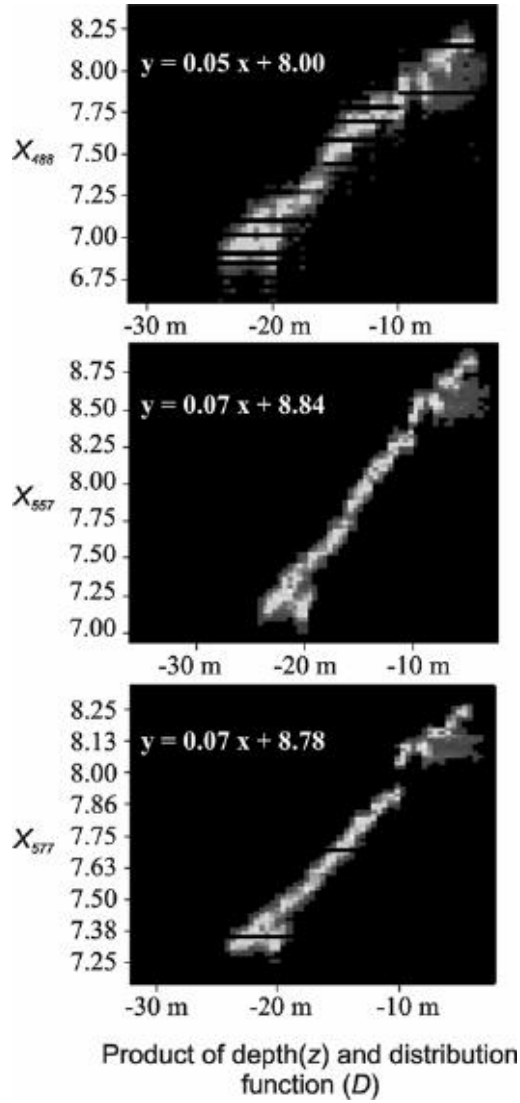
◀

Fig. 3 Plot of product of depth (z) and distribution function for light in water (D), and derivative bands (X_i) over sand bottom. The linear equation for the relationship in each band (i) is *inset* in the graph. The slope is equal to the water-attenuation coefficient (κ) in that band. The intercept is ln ($L_b - L_w$), the natural log of bottom radiance minus the deep-water radiance for sand in that band. Greater number of data points are shown by *dark grey shading* in the linear regression, while fewer data points are shown as *lighter shades of grey*. The occasional *horizontal line* on the graph results from missing data

corrections in the radiative transfer model are applied. The 577-nm band does not display the expected reflectance pattern and radiative transfer corrections do not improve the relative difference at overlapping regions. Due to Rayleigh scattering, the reflectance values in images at this wavelength decrease instead of increasing when the sun is higher in the sky. For this reason, and also since the water-attenuation coefficients for the 551- and 577-nm bands are the same (Table 1), results for depth and bottom type are predicted using the "differencing" method [Eqs. (3) and (5)] on the 488- and 551-nm bands only.

Depth prediction

A median of 89% and a mean of 86% accuracy in predicted depth [$z_{488/551}$, Eq. (5)] are achieved in waters at depths to 30.5 m within the study area (Fig. 4). Percent error in predicted depth is not related to depth ($R = 0.21$). Errors are no greater at shallow depths, for example. Large errors are present along the boundaries of the sand channel and sand fields. These errors may result from shadows cast by steep bathymetric gradients at low sun-elevation angles.

The radiative transfer model assumes a homogeneous water column, so large errors in predicted depth not found along margins may be caused by differences in water quality. Ocean water quality varies with the amount of sediment or organic detritus in suspension. In addition, the model assumes that reflectance of

regions of images. The relative difference in overlapping regions improves from 7 to 0.9% in the 488-nm band and from 4 to 0.7% in the 551-nm band, after

Table 2 Estimated or calculated sun-angle dependent or non-wavelength-dependent parameters in physical model

Variable	Symbol	Details	Reference
Distribution coefficient	D	$D = Dd + Du$ $Dd = fDa\_sun + = 1 + f = \ Da\_ska$ $Dd\_sky = 1.2$ $D_{d\_sun} = \dfrac{1}{\cos\theta_{sw}}$ $D_u = 1/\cos\theta_{rw}$	Gordon (1989)
Ratio of direct to total irradiance	f	0.66	Gregg and Carder (1990)
Downwelling air–water transmission coefficient	$T(\alpha \rightarrow w)$	$T(\alpha \rightarrow w) = fT_{sun} + (1-f)T_{sky}$ $T_{sky} = 0.934$ $T_{sun} = 1 - r(\theta_{sa} \rightarrow \theta_{sw})$ $r = $ Fresnel reflectance	Burt (1954)
Upwelling water–air transmission coefficient	$t(\theta_{cw} \rightarrow \theta_{ca})$	$t(\theta_{cw} \rightarrow \theta_{ca}) = 1 - r(\theta_{cw} \rightarrow \theta_{ca})$ $r = $ Fresnel reflectance	
Conversion factor, irradiance to radiance	Q	π	Mobley (1994)
Refractive index of water	n_w	1.334	Mobley (1994)

Table 3 Error matrix for multi-spectral percent living coral map. Ground reference data (line-intercept transects) are in the *columns* and percent living coral categories are in the *rows*. Overall accuracy, number of correctly classified ground reference points divided by total number of reference points, is shown. Producers' accuracy is calculated as the *diagonals* divided by *column totals*. Division of the *diagonals* by *row totals* results in the users' accuracy

		Reference data						
		< 15%	15–25%	25–40%	40–75%	> 75%	Sand	Total
Classified data	< 15%	4	1	0	0	0	0	5
	15–25%	1	2	0	0	0	0	3
	25–40%	0	0	2	0	0	0	2
	40–75%	1	1	3	14	3	0	22
	> 75%	0	0	0	0	5	0	5
	Sand	0	0	0	0	0	7	7
		6	4	5	14	8	7	44

Overall accuracy = (4 + 2 + 2 + 14 + 5 + 7)/44 = 77%

Producers' accuracy				Users' accuracy		
< 15%	4/6	67%		< 15%	4/5	80%
15–25%	2/4	50%		15–25%	2/3	67%
25–40%	2/5	40%		25–40%	2/2	100%
40–75%	14/14	100%		40–75%	14/22	64%
> 75%	5/8	63%		> 75%	5/5	100%
Sand	7/7	100%		Sand	7/7	100%

bottom type is the same (or the difference is negligible) in the two spectral bands. Examples of spectra of coral, algae and sand can be found in Hochberg and Atkinson (2000) as well as Holden and LeDrew (1999). Where errors in predicted depth are large, this assumption about bottom reflectance may be the reason.

Bottom-type prediction

Bottom-type solutions from multi-spectral data reflect benthic habitat (Lyzenga 1981; Mumby et al. 1997). In a study performed by Harney (2000) in Kailua Bay, seven benthic zones were mapped based on PLC as determined from 30-m line-intercept transects. The multi-spectral bottom-type coefficient map made from the "differencing" method on the 488- and 551-nm bands [$Y_{488/551}$, Eq. (3)] is clustered with unsupervised classification into seven categories (Fig. 5). Seventy-seven percent overall accuracy is achieved for the multi-spectral PLC map, i.e., 34 of the 44 PLC values derived from the 30-m line transects were correctly classified. Accuracy for individual classes is shown with producers' and users' accuracy. Users' accuracies are greater than the producers' accuracy. Producers' accuracies are 67% for the < 15% living coral category, 50% for the 15–25% living coral category, 40% for the 25–40% living coral category, 100% for the 40–75% living coral category, 63% for the > 75% living coral category, and 100% for sand. There is a positive correlation between the producers' accuracy and the number of reference points (line-intercept transect data) in that category ($R = 0.73$). Users' accuracies are 80% for the < 15% living coral category, 67% for the 15–25% living coral category, 64% for the 40–75% living coral category, 100% for the 40–75% living coral category, 100% for the > 75% living coral category, and 100% for sand.

Some reference points are not correctly classified in Fig. 5A, and it may appear that this occurs more than 77% of the time. However, this is not the case. With the complete coverage that multi-spectral data provides for mapping, we can resolve more detail than attained in the map based on PLC from 44 transect measurements alone (Fig. 5B). This detail is why the predicted PLC map looks different from the map in Harney (2000). In our predicted PLC map, most of the reference points fall well within or on the boundaries of their mapped categories. However, some of the reference points fall in an area that is narrow (4–5 pixels wide). These points are along the walls of the sand channel where the habitats of PLC can change over a small area.

Discussion

By improving our understanding of the relationship of coral reefs ecosystems and sedimentary systems with local and global environmental controls, we can improve efforts to manage these systems. The radiative transfer methods described in this paper can be used to extract useful information from multi-spectral data with minimal in situ measurements. Bathymetry and PLC can be mapped and the results from multiple surveys can be compared.

The solutions for depth and bottom type used in this paper are tested on two bands (488 and 557 nm) because we are working with data from a sensor that collected three bands and the third (577 nm) was not useful. The results mapped for depth and bottom type are remarkable since they are derived from two bands alone. Better
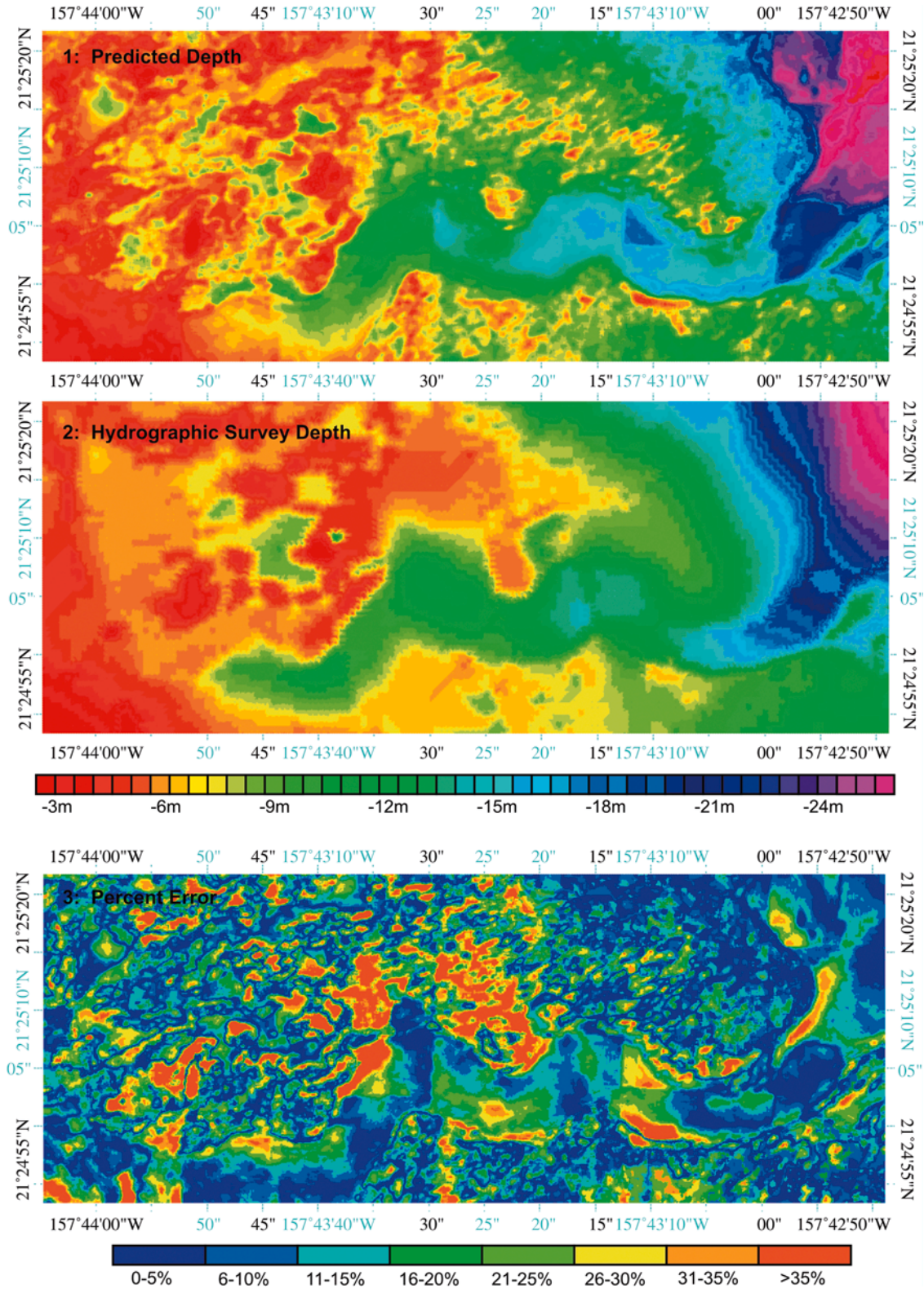
Fig. 4 Predicted depth, measured depth, and percent error in predicted depth. *Top panel* shows predicted depth from the multi-spectral wavelengths 488 and 551 nm [$z_{488/551}$, Eq. (3)]. *Middle panel* is depth determined from a USGS hydrographic survey. The multi-spectral predicted depth map is resampled to 15 m, the postion resolution of the hydrographic survey data. *Bottom panel* is percent error in predicted depth

discrimination of bottom type and greater accuracy in depth prediction will be possible when these methods are applied to hyperspectral systems, i.e., remote-sensing systems with many wavelengths. Some hyperspectral systems have hundreds of bands.

The radiative transfer model

We estimate atmospheric parameters in the radiative transfer model from published measurements taken under conditions thought to be similar to those of our experiment and our data set. Results will be improved for future studies if site-specific atmospheric measure-ments are made. Downwelling irradiance can be mea-sured with an irradiance meter and the fraction of downwelling irradiance due to the direct component (f) measured by putting a hat over the irradiance meter (Gordon 1989). A black target at the ocean surface, larger than the minimum discernable unit (MDU), should be used to better estimate haze, H, since roads and roofs of buildings are not black.

Accounting for a non-homogeneous water body in the radiative transfer model would result in improved depth and bottom-type predictions. To minimize the effect of water-quality differences, we chose to fly the data used in this study under the best possible weather and, therefore,

Fig. 5 A Bottom-type map derived using multi-spectral bands 488 and 551 nm [$Y_{488/551}$, Eq. (4)]. The multi-spectral PLC map is resampled to 30 m in agreement with line-intercept transect mapping data. **B** Percent living coral zone boundaries. (After Harney 2000.) *Numbers* show PLC at ground-truth points
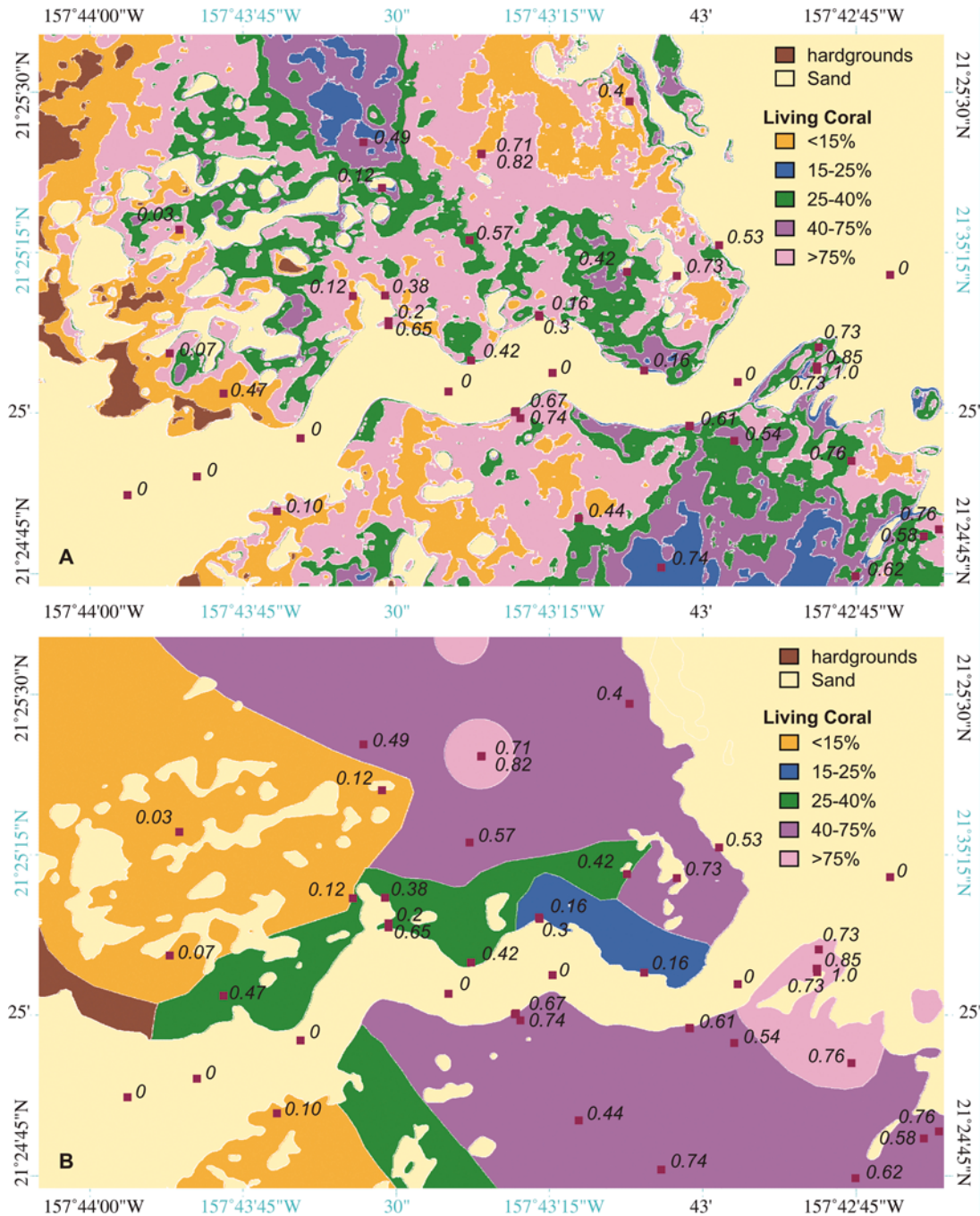
ocean conditions. On the day we collected the multi-spectral data, the water was clear in most of Kailua Bay. Even under these conditions, divers noted plumes of suspended sediment in portions of the bay.

Over most of the mapped area, the water was clear, and the radiative transfer methods and multi-spectral wavelengths worked well to predict depth and PLC. In those areas where the water column had suspended sediment (and at shallow depths), a combination of shorter wavelengths will perform better to predict depth and bottom type. Shorter wavelengths with increased water attenuation will be less affected by scattering from particles in the water (Mobley 1994). The ability to use different combinations of wavelengths in the solutions for depth and bottom type based on the water quality and depth in the study area is one reason why better predictions are possible where more wavelengths are available, such as with hyperspectral systems.

Some independently measured depth data are necessary to run the radiative transfer model. At least three georeferenced depth points over sand areas and at least another three points over known habitats on the reef are needed. The three-point minimum allows for linear regressions of the derivative channels, X_i, to measured depth so we can determine water-attenuation coefficients. Points where depth is measured (with latitude and longitude) can also be used to georegister the multi-spectral image mosaic.

Depth prediction

Whereas there are other ways of producing bathymetric maps, doing so using multi-spectral data is still a viable alternative. In general, mapping large areas quickly with specific survey objectives using multi-spectral sensors can be cheaper than hyperspectral sensors because the equipment costs are lower and the data reduction costs are less. However, advances in technology are making hyperspectral data increasingly cost effective.

Shallow depths do not curtail data collection in multi-spectral remote sensing to map bathymetry as with depth-mapping mechanisms aboard ships. There is complete and extensive coverage when mapping depth with multi-spectral data, unlike other forms of depth surveys that only cover a small area or leave out large sections of the study site (e.g., hydrographic surveys, LIDAR).

Percent living coral

Maps of PLC made from multi-spectral data using radiative transfer methods described in this paper can be used as baseline maps for coral reef monitoring. Regular PLC mapping will provide information on how reefs change through time. The radiative transfer model corrects for sun-angle dependent parameters, and atmospheric and water quality variables are determined for the day of data collection, so bottom-type coefficients from multiple days can be compared. Statistical reports of quantitative spatial change in marine sedimentary and living environments derived from multi-spectral data can be monitored and correlated to climate and anthropogenic activity, which is useful to managers of coastlines.

With predicted depth maps made from multi-spectral data, novel insights and analyses of ocean floor geology and ecology are possible: for example, maps of reef slope. From these maps, we can begin to analyze the relationship of slope to PLC (Fig. 6). The total area covered by the PLC categories can be assessed (Table 4). Finally, with detailed ecological ground control data (Harney 2000) and a good understanding of the geological dynamics in Kailua Bay, correlations among habitat types and coral and algal species to depth, slope, and coverage area can be made.

The >75% living coral category is the most spatially abundant coral category, making up 25% of the area studied, about 0.9 km^2. Covering 12 and 15% of the PLC map, respectively, the <15% living coral and 25–40% living coral categories are the next most extensive
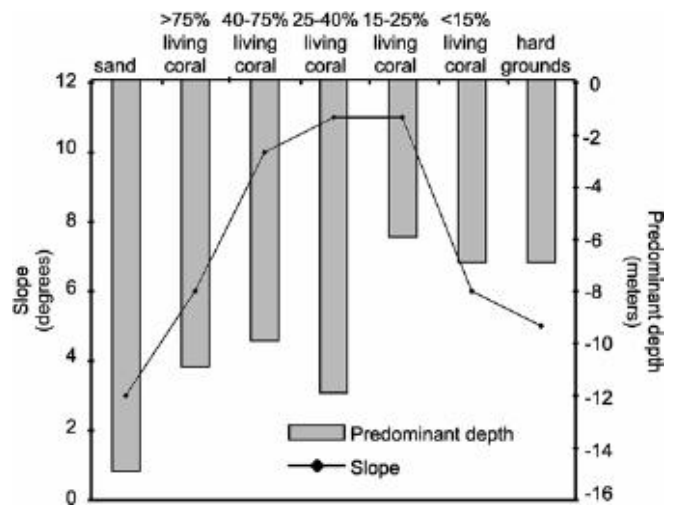

Fig. 6 Predominant depth and mean slope for PLC categories. Predominant depth, in meters, is taken as the peak of the histogram for depth in that category, and median and maximum slopes are in degrees for coral cover categories, hardgrounds, and sand

Table 4 Area (in m^2) and percent of study area covered by nearshore hardgrounds, sand, and the percent living coral categories

Category	Percent of study area	Area (m^2)
Nearshore hardgrounds	2	76,737
Sand	38	1,569,335
<15% living coral	12	493,977
15–25% living coral	3	123,939
25–40% living coral	15	602,851
40–75% living coral	7	290,670
>75% living coral	25	924,777

categories. With spatial areas of less than 10%, the nearshore hardgrounds, 15–25% living coral, and 40–75% living coral categories are the least spatially abundant. Sand and fossil reef hardgrounds make up almost 40% of the study area and have the most extensive depth range to 30 m.

Throughout Kailua Bay (i.e., in all PLC categories), *Montipora patula* occurs the most (Fig. 7; Harney 2000). This encrusting coral species (Fig. 8) is usually found growing among other corals (Fielding and Robinson 1993; Russo 1994), which accounts, in the line-intercept transect data, for why the counts of this species are greatest. *M. patula* is used as the species for comparison in all abundance ratios reported in the following discussion.

Abundance is calculated as the number of occurrences (count) of a given coral species divided by the number of transects in that category. It is interesting, however, that *M. patula* is recorded as being common in shallow water (below 3 m) (Fielding and Robinson 1993; Russo 1994), but in Kailua Bay this species is found throughout the depth range of the study area (Harney 2000). Coral reef habitats in Kailua Bay are found in depths to 23 m, with about the same standard deviation in depth in all habitats (mean $\sigma = 4$) (Table 5).
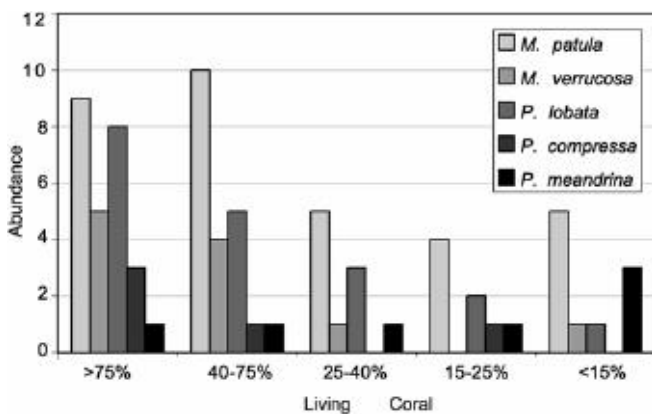

Fig. 7 Abundance of coral species in PLC categories. [Abundance is an average. It is the number of occurrences (count) of a given species divided by the number of transects in that category.] (After Harney 2000)
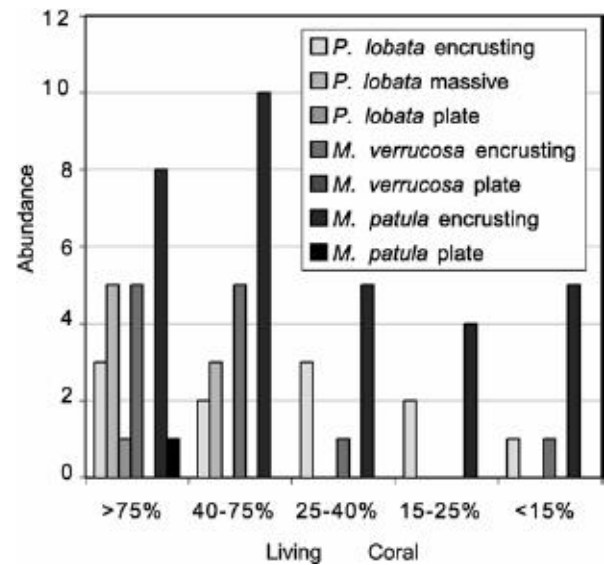

Fig. 8 Abundance of coral morphologies for *Porites lobata*, *Montipora verrucosa*, and *Montipora patula* species in PLC categories. (After Harney 2000)

A map of the slope for every pixel in the multispectral mosaic was generated from the predicted depth map. Analyzing the maps of slope and bottom type, we find that gentle slopes (mean of 5°, maximum 42°) are found in the most prolific and least prolific living coral categories (>75 and $<15\%$ living coral). The middle PLC categories exhibit steeper slopes, averaging 11° (maximum 60°). We present two hypotheses for this relationship among PLC and slope.

The first hypothesis is that the relationship between slope and PLC is based on the underlying topography on which a coral habitat grows. In other words, slope appears to be the inhibiting factor to PLC cover. The second hypothesis is that the relationship between slope and PLC is a function of the large-scale rugosity of a given coral reef habitat. Theses two hypotheses can be tested in the future. In the following paragraphs, the hypotheses are described in more detail.

There is ecological support of the first hypothesis, that basement topography is the reason we see the >75 and $<15\%$ living coral categories on gentle slopes. The most abundant coral species in the $>75\%$ living coral

Table 5 Minimum and maximum depth (in m) and standard deviation of depth range for percent living coral categories, hardgrounds, and sand

Category	Minimum depth (m)	Maximum depth (m)	Standard deviation of depth (s)	Predominant depth (m)	Mean slope (°)	Maximum slope (°)
Hardgrounds	−6.0	−19.0	1.2	−7	5	35
<15% living coral cover	−4.6	−19.8	3.9	−7 and −13 to −15	6	40
15–25% living coral cover	−1.4	−23.8	5.0	−6	11	60
25–40% living coral cover	−1.1	−22.6	4.0	−12	11	47
40–75% living coral cover	−0.61	−22.7	3.6	−10	10	55
>75% living coral cover	−2.9	−22.6	3.7	−11 to −16	6	42
Sand	−0.94	−30.5	12.1	−15 to −25	3	46

category is *P. lobata* which does well on well-lit, gentle reef slopes (Fielding and Robinson 1993; Russo 1994). In contrast, *P. meandrina* is the most abundant species in the <15% living coral category. This coral species is commonly found in shallow waters where there are strong currents or wave action (Fielding and Robinson 1993; Russo 1994). Such shallow, wave-eroded reef platforms have gentle slopes.

However, there is a bimodal depth distribution in the <15% living coral category. One area where we find the <15% living coral category is in the *P. meandrina*-dominated, wave-eroded, nearshore, shallow (<7-m) habitat mentioned above. The second <15% living coral cover habitat is found in deep water (13–15 m), north of the sand channel. Since *P. meandrina* are the first to colonize (Fielding and Robinson 1993; Russo 1994), the high occurrence of *P. meandrina* in deep water may be evidence of succession. That is, the rehabitation of coral from a previously more prolific growth state that may have been destroyed or damaged by a significant event such as large wave stress or human activity.

The middle PLC categories are found in two general areas: (1) along the slopes of the sand channel, and (2) north and south of the sand channel on spur-and-groove coral reef features. The water-incised sand channel walls and spur-and-groove geomorphology create steep bathymetric slopes. This first hypothesis suggests that these middle PLC categories are less prolific than the >75% living coral category because they are found on these steep geological gradients in the Bay.

The second hypothesis suggests that the slopes are an inherent quality of the PLC habitat, i.e., the slope is a measure of the topography of the habitat. We explain that slopes are gentle in the >75% living coral habitat because, in these habitats, corals are prolific and have filled in all available space laterally and horizontally. A fully grown and filled-in coral garden has an overall gentle slope on its surface.

The <15% living coral habitats exhibit gentle slopes due to erosion of topography. This erosion occurs either due to constant wave activity on the shallow reef platform or due to periodic large-scale events. Erosion clears out any large coral colonies that might cause steep bathymetric gradients. Corals in these habitats may be low-lying and encrusting forms or small colonies, like those formed by *P. meandrina* species.

In the middle PLC habitats, coral growth has not completely filled in the three-dimensional spaces on the reef, i.e., there are still spaces in the bathymetry of the reef habitat. This results in steep slopes between large coral colonies or communities of clustered colonies, for example.

The low producers' accuracy in some PLC categories is a result of the small number of transect reference points in those categories. The more important categorical accuracy estimate is the users' accuracy as this determines the probability of a user going to a given place on the bottom-type map and finding a particular PLC there. All users' accuracies are improved over the producers' accuracies, except the 40–75% living coral category. There are the most ground truth points plotted within this category that should have been allocated to other categories (data in the row of the error matrix, category 40–75%). This is because the details of other categories within the 40–75% category were lost during the resampling of the multi-spectral image to 30-m resolution to fit the line-transect data resolution.

Bottom reflectance, A (see Appendix), can be directly solved for, instead of solving for bottom-type coefficients, by using the multi-spectral predicted depth, z, or depth measured by other means, in the radiative transfer model (Eq. A2). This is useful since reflectance measured with a field radiometer can be used to train supervised classification of predicted bottom reflectance multi-spectral maps. Reflectance spectra for coral reefs from field radiometer measurements are being made (Holden and LeDrew 1999; Hochberg and Atkinson 2000) and may become available in spectral libraries in the future. The use of radiometer-measured coral reef reflectance to train remotely sensed bottom albedo will be particularly useful with hyperspectral data where many wavelengths of reflected sunlight (in contrast to three in this study) are measured. The greater number of bands measured in hyperspectral remote sensing gives a spectrum of sensor-measured reflectance (in multiple layers of digital band maps) to train with a spectrum of field radiometer-measured reflectance. Hence, the shape of the reflectance spectrum for each bottom type as well as the strength of the reflectance signal in a given band are used to solve for the bottom type.

Although field-measured reflectance to perform supervised classification on remotely sensed data has been in use on land for some time, this approach in marine environments is still in its infancy. One reason is that the minimum discernable unit for multi-spectral data is larger than the size of individual coral species, so spectra should be a measure of habitat type rather than species until greater resolution is achieved. In addition, this approach has not been used extensively in marine environments, because the correction of remotely sensed data for the effects of the ocean is in an early stage of development. However, researchers are working on measuring spectral reflectance of habitats with field radiometers (e.g., Holden and LeDrew 1999), and sensors able to acquire greater resolution will be developed in the future.

Conclusions

1. The radiative transfer model and estimated parameters used in this paper are sufficient to normalize multi-spectral images in a mosaic to one another and can be used with any passive airborne remote sensing digital data.
2. Bathymetry and PLC are appropriately mapped from two bands of multi-spectral data (488 and 551 nm) using the "differencing" method we present in this paper.

3. Spatial change in depth and PLC can be mapped through time with multi-spectral data using the methods described in this paper and if additional multi-spectral data sets are collected at different dates.
4. The greatest PLC habitats are found on reef tops where gentle slopes are observed. Gentle slopes are also observed in the least PLC habitats. In contrast, the medium PLC habitats are associated with steeper reef slopes.

Appendix A: Significant symbols

A	Irradiance reflectance (albedo) of the ocean bottom (sr^{-1})
A_{T_a}	Atmospheric transmittance from space to the ocean surface (0 to ∞)
A_{T_c}	Atmospheric transmittance from the ocean surface to the multi-spectral sensor (0 to h_c)
D	Distribution function for the underwater light field
D_d	Distribution function for the downwelling underwater light field
D_{d_sky}	Distribution function for the diffuse component of the downwelling underwater light field
D_{d_sun}	Distribution function for the direct component of the downwelling underwater light field
D_u	Distribution function for the upwelling underwater light field
E_d	Downwelling irradiance (W m^{-2} nm^{-1})
f	Fraction of direct sunlight to total sunlight in the incident radiation transmitted through the air–water interface
F_0	Extraterrestrial irradiance corrected for earth–sun distance and orbital eccentricity (W m^{-2} nm^{-1})
H	Path irradiance due to scattering by particles in the atmosphere between the ocean surface and the airplane (W m^{-2} nm^{-1})
L_b	Ocean bottom radiance (W m^{-2} nm^{-1} sr^{-1})
L_d	Radiance measured at the multi-spectral detector [Eqs. (A3) and (A4)] (W m^{-2} nm^{-1} sr^{-1})
L_w	Radiance of the ocean (W m^{-2} nm^{-1} sr^{-1})
n_w	Refractive index of water
Q	Conversion factor for irradiance to radiance
R_∞	Irradiance reflectance of the ocean (sr^{-1})
$T(a \rightarrow w)$	Transmission coefficient for downwelling irradiance across the air–water interface
T_{sun}	Transmission coefficient for the direct component of downwelling irradiance across the air–water interface
T_{sky}	Transmission coefficient for the diffuse component of downwelling irradiance across the air–water interface
$t(\theta_{cw} \rightarrow \theta_{ca})$	Snell transmission coefficient for radiance to the camera across the water–air interface
κ	Water-attenuation coefficient (m^{-1})
$\tau_A, \tau_R, \tau_{Oz}$	Optical extinction coefficients for aerosol, Rayleigh and ozone scattering for the distance from the ocean surface to the sensor (km^{-1})
$\tau'_A, \tau'_R, \tau'_{Oz}$	Optical extinction coefficients for aerosol, Rayleigh and ozone scattering for the atmosphere from space to earth (km^{-1})
θ_{sa}	Solar zenith angle in air
θ_{sw}	Solar zenith angle in water
θ_{ca}	Camera zenith angle in air
θ_{cw}	Camera zenith angle in water

Appendix B: Radiative transfer theory

Following Philpot (1989), the irradiance reflectance, $R(z)$, is the ratio of upwelling irradiance to downwelling irradiance:

$$R_{rs} = \frac{E_u(z)}{E_d(z)} \tag{A1}$$

For a given wavelength, $\lambda_{i,}$ the reflectance just beneath the water surface, $R(0^-)$, can be written as

$$= (A(i) - R_\infty(i)) \exp^{-\kappa(i)Dz} + R_\infty(i) \tag{A2}$$

where bottom albedo, A, is the value of R just above the bottom; R_∞ is the value of $R(0^-)$ for an infinitely deep ocean; κ is a water-attenuation coefficient; and D is the distribution function for the underwater light field.

In a comprehensive formula that includes transmission across the air–water interface, atmospheric effects, solar illumination, and the conversion of irradiance to radiance, the upwelling radiance measured at the multi-

Fig. 9 Components of the radiative transfer model
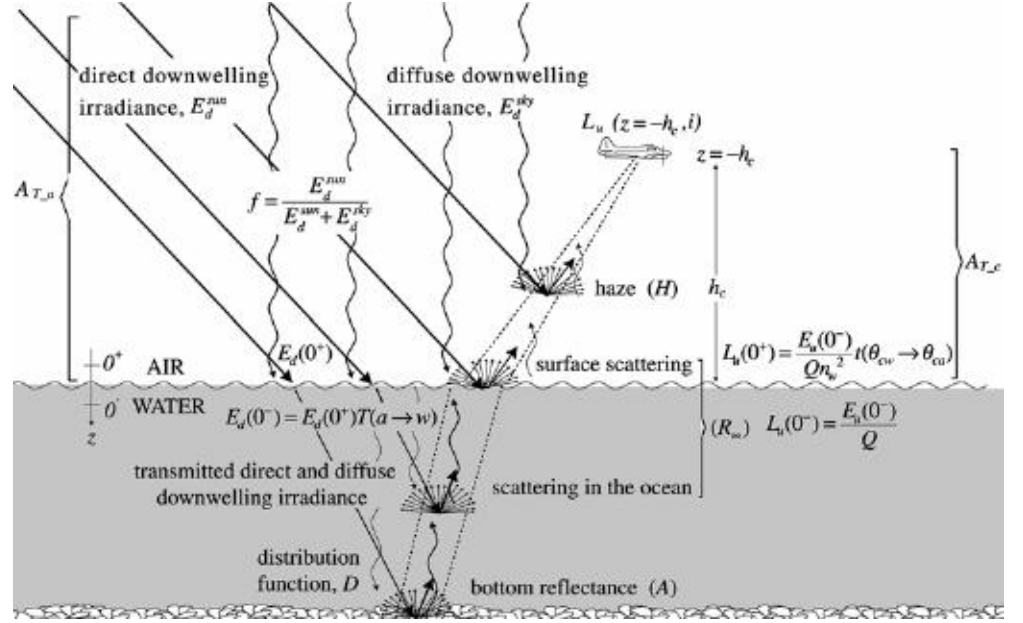
spectral camera, L_u, for a given wavelength, λ_i, is written as:

$$L_d(z = -h_c, i)$$

$$= E_d(0+,i)A_{Tc}(i)\left\{\frac{T(a \to w)\, t(\theta_{cw} \to \theta_{ca})R(0-,i)}{Qn_w^2} + H(i)\right\}$$

$$\text{Wm}^{-2}\text{nm}^{-1}\text{sr}^{-1} \tag{A3}$$

in which h_c is the height of the camera above the sea surface and $E_d(0^+)$ is the total downwelling irradiance, attenuated by the atmosphere, just above the ocean surface (Fig. 9). $E_d(0+)$ is given by $E_d(0+) = (\cos\theta_{sa}F_o(i)A_{T\_a})/f$ where $F_o(i)$ is extraterrestrial irradiance corrected for earth–sun distance and orbital eccentricity (Gregg and Carder 1990) and f is the fraction of total downwelling light due to the direct component, i.e. the ratio of irradiance due to sunlight to irradiance of sunlight plus skylight. A_{T_a}, the atmospheric transmission for the height of the atmosphere (from the ocean surface to space), involves the exponent of optical extinction coefficients, τ'_A, τ'_R, and τ'_{Oz}, for aerosol, Rayleigh, and ozone scattering and absorption in the atmosphere, respectively. $A_{Ta} = \exp^{-\left[\tau'_A + \tau'_R + \tau'_{Oz}\right]/\cos\theta_{sa}}$ where θ_{sa} is the incident, zenith sun angle (sa = sun in air).

H is path radiance due to scattering by particles in the atmosphere between the ocean surface and the airplane. A_{T_c} is the atmospheric transmittance back to the camera. With optical extinction coefficients for the distance from the ocean surface to the altitude of the airplane (0 to h_c), $A_{T\_c} = \exp^{-\left[\tau_A + \tau_R + \tau_{Oz}\right]/\cos\theta_{ca}}$ where θ_{ca} is the transmitted, zenith bottom-reflectance angle (ca = camera path in air).

$T(a \to w)$ is the transmission coefficient for downwelling irradiance across the air–water interface. $\frac{t(\theta_{cw} \to \theta_{ca})}{n_w^2}$ is

the transmission coefficient for upwelling radiance across the water–air interface, and θ_{cw} is the incident, zenith bottom-reflectance angle (cw = camera path in water). Q is a conversion factor for irradiance to radiance, which for our calculations can be taken to have the value π, and n_w is the index of refraction for water.

Equation (A3) can be written in the simplified form

$$L_d = L_b \exp^{-gz} + L_w \tag{A4}$$

if L_d, the radiance measured at the multi-spectral detector, is defined as

$$L_d \equiv \left(\left(\frac{L_u}{E_d(0+)A_{T\_c}}\right) - H\right)\Big/ C_0 \tag{A5}$$

where $C_0 = \frac{T(a \to w)\, t(\theta_{cw} \to \theta_{ca})}{Qn_w^2}$; L_b is the bottom-type radiance; L_w is the radiance of the water column; and g is defined as the product of the water-attenuation coefficient, κ, and the distribution function, D, given by $g \equiv \kappa D$.

References

Bainbridge SJ, Reichelt RE (1988) An assessment of ground truthing methods for coral reef remote sensing data. Proc 6th Int Coral Reef Symp 2:439–444

Burt WV (1954) Albedo over wind-roughened water. J Meteorol 11:283–290

Congalton RG, Green K (1999) Assessing the accuracy of remotely sensed data: principles and practices. Lewis, Boca Raton, 137 pp

Coyne MA, Fletcher CH, Richmond BM (1999) Mapping coastal erosion hazard areas in Hawai'i: observations and errors. J Coast Res 28:171–184

Elterman L (1968) UV, visible and IR attenuation for altitudes to 50 km, 1968. National Technical Information Service, Springfield, 57 pp

Fielding A, Robinson E (1993) An underwater guide to Hawai'i. University of Hawai'i Press, Honolulu, 156 pp

Gordon HR (1989) Dependence of the diffuse reflectance of natural waters on the sun angle. Limnol Oceanogr 34:1484–1489

Gordon HR, Brown OB (1973) Irradiance reflectivity of a flat ocean as a function of its optical properties. Appl Opt 12:1549–1551

Gordon HR, Brown OB (1974) Influence of depth and albedo on the diffuse reflectance of a flat homogeneous ocean. Appl Opt 13:2153–2159

Gordon HR, McCluney WR (1975) Estimation of the depth of sunlight penetration in the sea for remote sensing. Appl Opt 14:413–416

Green EP, Mumby PJ, Edwards AJ, Clark CD (1996) A review of remote sensing for the assessment and management of tropical coastal resources. Coast Manage 24:1–40

Gregg WW, Carder KL (1990) A simple spectral solar irradiance model for cloudless maritime atmospheres. Limnol Oceanogr 35:1657–1675

Harney JN (2000) Carbonate sedimentology of a windward shoreface: Kailua Bay, Oahu, Hawaiian Islands. PhD Thesis, Department of Geology and Geophysics, University of Hawai'i, Honolulu, 232 pp

Harney JN, Grossman EE, Richmond BM, Fletcher CH (2000) Age and composition of carbonate shoreface sediments, Kailua Bay, Oahu, Hawai'i. Coral Reefs 19:141–154

Hochberg EJ, Atkinson MJ (2000) Spectral discrimination of coral reef benthic communities. Coral Reefs 19:164–171

Holden H, LeDrew E (1999) Hyperspectral identification of coral reef features. Int J Remote Sensing 20:2545–2563

Kirk JT (1991) Volume scattering function, average cosines, and the underwater light field. Limnol Oceanogr 36:455–467

Lee Z, Kendall LC, Hawes SK, Steward RG, Peacock TG, Curtis OD (1994) Model for the interpretation of hyperspectral remote-sensing reflectance. Appl Opt 33:5721–5732

Lyzenga DR (1977) Reflectance of a flat ocean in the limit of zero water depth. Appl Opt 16:282–283

Lyzenga DR (1978) Passive remote sensing technique for mapping water depth and bottom features. Appl Opt 17:379–383

Lyzenga DR (1981) Remote sensing of bottom reflectance and water attenuation parameters in shallow water using aircraft and Landsat data. Int J Remote Sensing 2:71–82

Maracci G (1985) Results of atmospheric optical measurements at two sites on the Cape West Coast. In: Channon LV (ed) South African Ocean Colour and Upwelling Experiment. Sea Fisheries Research Institute, Cape Town, pp 171–175

Maragos JE, Grober-Dunsmore R (eds) (1998) Proceeding of the Hawai'i Coral Reef Monitoring Worksh, East-West Center, Honolulu, 334 pp

Maritorena S (1996) Remote sensing of the water attenuation in coral reefs: a case study in French Polynesia. Int J Remote Sensing 17:155–166

Mobley CD (1994) Light and water: radiative transfer in natural waters. Academic Press, San Diego, 592 pp

Mumby PJ, Green EP, Edwards AJ, Clark CD (1997) Coral reef habitat-mapping: how much detail can remote sensing provide? Mar Biol 130:193–202

Mumby PJ, Green EP, Clark CD, Edwards AJ (1998) Digital analysis of multispectral airborne imagery of coral reefs. Coral Reefs 19:59–69

Paredes JM, Spero RE (1983) Water depth mapping from remote sensing data under generalized ration assumption. Appl Opt 22:1134–1135

Philpot W (1989) Bathymetric mapping with passive multispectral imagery. Appl Opt 28:1569–1578

Russo R (1994) Hawaiian reefs: a natural history guide. Lorraine Press, Salt Lake City, 174 pp